





## Filament displacement image analytics tool for use in investigating dynamics of dense microtubule networks


Nicholas J. Mennona <sup>1,2,3</sup>, Anna Sedelnikova <sup>4</sup>, Ibtissam Echchgadda <sup>1</sup>, and Wolfgang Losert <sup>2,3</sup>

<sup>1</sup>*Air Force Research Laboratory, Radio Frequency Bioeffects Branch, JBSA Fort Sam Houston, Texas 78234, USA*

<sup>2</sup>*Institute for Physical Science and Technology, University of Maryland, College Park, Maryland 20742, USA*

<sup>3</sup>*Department of Physics, University of Maryland, College Park, Maryland 20742, USA*

<sup>4</sup>*Science Applications International Corporation, JBSA Fort Sam Houston, Texas 78234, USA*

 (Received 17 February 2023; revised 15 July 2023; accepted 24 August 2023; published 29 September 2023)

The fate and motion of cells is influenced by a variety of physical characteristics of their microenvironments. Traditionally, mechanobiology focuses on external mechanical phenomena such as cell movement and environmental sensing. However, cells are inherently dynamic, where internal waves and internal oscillations are a hallmark of living cells observed under a microscope. We propose that these internal mechanical rhythms provide valuable information about cell health. Therefore, it is valuable to capture the rhythms inside cells and quantify how drugs or physical interventions affect a cell's internal dynamics. One of the key dynamical entities inside cells is the microtubule network. Typically, microtubule dynamics are measured by end-protein tracking. In contrast, this paper introduces an easy-to-implement approach to measure the lateral motion of the microtubule filaments embedded within dense networks with (at least) confocal resolution image sequences. Our tool couples the computer vision algorithm Optical Flow with an anisotropic, rotating Laplacian of Gaussian filtering to characterize the lateral motion of dense microtubule networks. We then showcase additional image analytics used to understand the effect of microtubule orientation and regional location on lateral motion. We argue that our tool and these additional metrics provide a fuller picture of the active forcing environment within cells.

DOI: [10.1103/PhysRevE.108.034411](https://doi.org/10.1103/PhysRevE.108.034411)

### I. INTRODUCTION

Microtubules (MTs) are stiff tubular filaments that comprise one of the main mechanical structures within eukaryotic cells, similarly to the actin cortex. Much research concerning MT dynamics focuses on the biochemical interactions involved with single filaments or in vitro networks of MTs [1–8]. However, MTs form cargo networks within a cell body (due to their high relative stiffness); in other words, MTs, enmeshed within a cell, must be regarded as a system from which information regarding entire cell functionality and health can be extracted. Indeed, quantifying this mechanical network is of interest since mechanical disruption of these highways affects cellular functionality [2,4,9–11]. In addition, other aspects of cellular mechanoregulation are assumed to functionally depend upon MT deformation [10,11]. One way to create such mechanical disruption is through the major chemotherapy drugs that aim to prevent cell division by targeting MTs, most notably Nocodazole and Paxitaxel, which destabilize and stabilize MTs, respectively [12–14]. Electric fields are also known to affect MT structure, since tubulin heterodimers are polar [15]; it is unknown whether electric fields drive oscillatory behavior of MT networks.

Typically, the analysis of MTs in cells requires labeling end-tip (EB) proteins. EB proteins are the end proteins of MT filaments that form cometlike trajectories; the straight trajectories of these ends allow one to quantify the dynamical instability (polymerization and/or depolymerization) which

characterizes MT behavior [16]. Moreover, algorithms exist, for example, PlusTipTracker [17], which allows one to quantify the trajectories of such comets. However, analysis of the dynamics of the MT filaments themselves in the literature is poorly defined. Given that the MT network is contained within a forcing environment (MTs respond to shear forcing, hydrodynamic forcing, and cytoskeletal force generation from kinesin and dynein; due to the high persistence length of MTs, thermal forcing is negligible [1–8]), the motion of the filaments will reflect the overall active forcing environment around the MT network within the cell. As a result, we retain a fuller picture of the internal rhythms of cellular mechanics than just focusing on the growth mechanics of MTs themselves.

Here we introduce a filament displacement image analysis method (FIDI) for quantifying lateral dynamics of MTs that form a dense network. The image processing algorithms combined in this method are anisotropic Laplacian of Gaussian filtering (LoG), a second-order edge detection algorithm, and optical flow (OF), a computer vision technique used to quantify local motion at close to the pixel scale [18,19]. In previous work, we used each of these tools separately. LoG filtering identified orientation organization in static actin filament networks [20] while OF quantified the dynamics of polymerized actin [21]. In this paper, we combine these algorithms (LoG+OF) for analyzing the dynamics of dense MT filament networks. Although super-resolution has shown to benefit researchers investigating cytoskeletal filaments [20,22], with

just confocal imaging our tool is still able to capture the motions of MTs embedded within the active forcing environment.

FIDI is distinct from other tools used for understanding bending dynamics of cytoskeletal filaments. Previous algorithmic tools have been developed to track filaments along their lengths and model the dynamics to quantify the persistence length and bending rigidity of cytoskeletal filaments. Indeed, other studies have devoted attention to the physical modeling of these filamentous networks [23,24]. Even if the density of the network renders individual filament tracking impossible, lateral motion of the constituent filaments in the MT network is still visible by eye. OF is not sufficient alone to quantify this motion since motion of two crossing filaments (frequently encountered in dense filamentous networks) will generate artifacts in the OF field. As we are not tracking filaments over time, LoG provides us with pixels belonging to a MT filament while OF measures the movement of detected pixels over time. In summary, we prefilter our data with LoG and then further measure with OF, which allows us to (1) identify pixels associated with MT filaments and (2) group filamentous pixels with similar angles, and then subsequently measure the lateral motion of such detected objects. Using additional image processing tools, we can separately analyze the motions of MT filaments depending upon the filament angle (generated as output from LoG filtering) and the region within cells.

## II. EXPERIMENTAL METHODS

### A. Cell culture

Rodent neuroblastoma-glioma cells [NG108-15 (108CC15) ATCC HB-12317, Manassas, VA] were cultured at 37 °C in a humidified 95% air, 5% CO<sub>2</sub> atmosphere in Dulbecco's Modified Eagle's Medium (DMEM, 11965-092, Invitrogen, Carlsbad, CA) containing no sodium pyruvate, 10% fetal bovine serum (FBS), 1 I.U./ml penicillin, 0.1 µg/ml streptomycin, 0.1 mM hypoxanthine, 400 nM aminopterin, and 0.016 mM thymidine. Cells were harvested between passages 20 and 30 and plated at a density of 104 cells/cm<sup>2</sup> on poly-D-Lysine (100 µg/ml, Sigma P7886) precoated glass-bottomed dishes (MatTek) in a serum-free medium consisting of DMEM, 1 mM dibutyl cyclic AMP (Millipore-Sigma), and antibiotics. Differentiation was induced 24 h after cell plating by replacing the growth medium with a differentiating medium in which the FBS had been substituted with B27 (Gibco 17504044) and supplemented with 1 mM dibutyl cAMP (Tocris 1141). The differentiating medium was replaced every 48 h. Cells were used for experiments after 7–14 days of differentiation. Differentiated cells exhibited spontaneous action potentials (APs), evoked by current injection in 50% and 70% of the cells at 10 days post differentiation. Chinese Hamster Ovarian-K1 (CHO-K1) was obtained from ATCC (Manassas, Virginia). CHO-K1 cells were cultured in an F12 K medium supplemented with 10% FBS, 2 mM l-glutamine, and 100 U/mL penicillin and/or streptomycin at 37 °C with 5% CO<sub>2</sub> in air. Plasmids and cellular transfection L304-EGFP-Tubulin-WT, which specifically labels tubulin, was a gift from Weiping Han (Addgene plasmid No. 64060[25];

RRID:Addgene No. 64060). Plasmid DNA was prepared using a Qiagen Plasmid Plus Maxi Kit (12963, Qiagen, Germantown, MD). For the lentiviral construct (L304-EGFP-Tubulin-WT), the plasmid was packaged into lentivirus and amplified to 108 infectious units (IFU)/ml.

### B. Generation EGFP-tubulin expressing lentivirus

The L304-EGFP-Tubulin-WT construct was packaged in pseudoviral particles in 293TN producer cells (SBI, LV900A-1); the supernatant containing pseudoviral particles was collected at 48 h post transfection, filtered at 0.45µm PVDF filters and centrifuged at 50 000Xg, 90 min at 4 °C. Then, pseudoviral containing precipitate was resuspended in a TNE buffer (50 mM Tris, pH 7.8, 130 mM NaCl, 1 mM EDTA), the virus was stored in 100 µl aliquots at –80 °C. Relative pseudoviral titer was determined by transducing cells and by counting the number of cells expressing EGFP-Tub, allowing 72 h for expression to start.

### C. Microscopy

Image sequences were acquired using the Leica TCS SP5. Confocal microscopy was performed with magnification of 40x water immersion objective. The conversion ratio from pixel to micron ranged from 0.04 to 0.15 microns/pix. Image sequences were acquired every 1.1 seconds, which is faster than previous studies [23]. Images analyzed were of strips of cells with image dimensions of 40 × 1024.

## III. RESULTS

### A. Anisotropic Laplacian of Gaussian filtering highlights MT filaments

The data used for prototyping the algorithm contains image sequences of Tubulin-GFP transfected NG108 cells as seen in Fig. 1(a). Within these cells, we observe by eye a dense network of microtubule filaments. These filaments are oriented in several different directions within the cell body as shown in the zoomed-in region in Fig. 1(b). After pre-processing with a Gaussian filter, we convolve these data with a rotating, anisotropic LoG kernel. Examples of rotations of the kernel are shown in Fig. 1(c) (different orientations, i.e., left-leaning, right leaning, and vertical, in addition to different shades and colors corresponding to different angles). Due to the bidirectional nature of the kernel, we rotate the kernel through  $\pi$  radians (as opposed to  $2\pi$  radians) at a discrete number of angles, a parameter chosen for accuracy and speed. Given data with  $N$  columns and  $M$  rows, the convolution results in a matrix with  $n$  columns and  $m$  rows, where  $n, m = N - p, M - p$  ( $p$  is defined as the padding size used to avoid artifacts). Edge effects occur when convolving close to the edges of data frames where the convolution is likely to extend beyond the image frame. We fix the padding at 6 pixels based upon observation of edge anomalies. Due to the nature of our data, as discussed later, we desire to retain as much filament information as possible. The kernel for this convolution is described in Eq. (1):

$$L(x, y) = \frac{-y^2 + \sigma_y^2}{\sigma_y^4} \exp\left(\frac{-x^2/\sigma_x^2 - y^2/\sigma_y^2}{4\pi\sigma_x\sigma_y}\right). \quad (1)$$

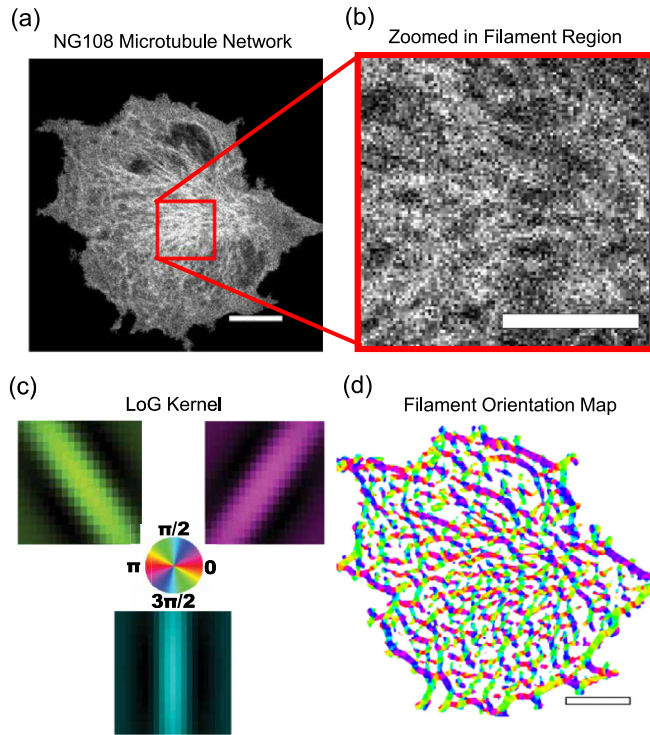


FIG. 1. LoG algorithm extracts MT filaments in every frame. (a) NG108 cell line with fluorescently labeled microtubule filaments. This confocal image displays a MT network with representative density of filaments. (b) Cytoskeletal networks containing filaments oriented in different directions. Even with the relatively low image resolution, the variety of microtubule orientations (some filaments are tilted while others are horizontal) is apparent. (c) Anisotropic, rotating Laplacian of Gaussian (LoG) filter with some rotation steps. The rods (right leaning, left leaning, and vertical) in each of the three images represent the LoG kernel with angle prescribed as the closest area on the color wheel (different shading represents different angles). These rods resemble the shapes of microtubules, which showcases how microtubules are detected. Note that once microtubule pixels are found above a threshold, each pixel is ascribed an associated angle belonging to which kernel causes maximal value in the max projection step. (d) Filament orientation map output from convolving data in (a) with kernel in (c). This final output shows all microtubule filaments detected. Note that there are spatial homogeneities with neighboring pixels which amounts to filament detection. Moreover, note that there are regions of white (corresponding to pixels not valued as microtubules) within the image; areas not white (different colors and shades) represent regions where the algorithm has identified a filamentous pixel and has prescribed an angle for this pixel. We found that LoG parameters of Refs. [1,7] for the sigma in  $\hat{x}$  and  $\hat{y}$  as well as 30 rotations work well with our data. Our scripts are provided in the GitHub link at the end of the paper. Scale bars are 10  $\mu\text{m}$  for (a) and (d); scale bar is 5  $\mu\text{m}$  for (b).

The anisotropy of the LoG kernel results from the quadratic prefactor and the different sigma parameters in the Gaussian. To achieve a rodlike object for extraction of filamentlike objects, we induce anisotropy in the minor axis ( $\hat{y}$ ) by penalizing for extending in that direction. Indeed, notice that higher values of  $y$  correspond to lower values of  $L$  in Eq. (1). This anisotropy causes the rapid dropoff as seen in Fig. 1(c) [notice

the color (shade) of the rod remains relatively constant while areas far away from the rod in the perpendicular direction are darker]. Additionally, the different sigma parameters,  $\sigma_x$  and  $\sigma_y$ , regulate the width of the kernel in  $\hat{x}$  and  $\hat{y}$ , which can vary the thickness of the rod, furthering the anisotropic effect. After convolution, a matrix with dimensions  $n,m,a$  results (where  $a$  is defined as the discrete number of angles chosen for kernel rotation); we have then  $a(N-p)\times(M-p)$  frames and we take the max projection of this matrix in the  $a$  dimension to arrive at our final output matrix. Finally, we threshold these maximal values to ensure they correspond to filaments. This output matrix contains pixels which (1) have been detected above the threshold and (2) have an angle, initially in the range  $[0, 2\pi]$ , associated with them. An example output is seen in Fig. 1(d), where the colors (shades) correspond to the angles in the color wheel in Fig. 1(c). Our LoG filtering detects filaments on a pixel basis. The use of pixel-by-pixel detection foregoes the difficulty in tracking a filament with fluctuating length and changing position over time. In this sense, the algorithm measures changes in motion but is agnostic as to which filaments are moving or had previously moved. Moreover, our pixel detection method allows us to detect with (sub)pixel accuracy MT fluctuation (even for a filament with fixed length). We optimize our filter threshold to select those pixels which belong to noticeable filaments and to minimize the detected edges which do not belong to filaments in the output data.

## B. Capturing lateral motion of detected MT filaments in dense networks using optical flow

We apply the Lucas-Kanade OF algorithm onto the pre-processed data. OF measures the spatial changes in image intensity over time, an example of applicable data for this algorithm is shown in Fig. 2(a). The algorithm detects pixel intensity changes between frames, as shown in Fig. 2(b), and spatially defines these intensity changes; as such we are given vectors that describe the motion. The OF output for the data shown in Fig. 2(a) is produced in Fig. 2(c). In this way, we can assess apparent motion within the fluorescently labeled cells. Outputs from OF are a magnitude and orientation matrix, which allow us to understand the speed of the motion as well as its direction. For a more detailed explanation of OF, please consult Ref. [21]. The equation for OF is referenced in Eq. (2). We store the magnitude and orientation output from convolution of the data set with OF. We use the filaments detected by LoG as a mask overlaid upon the OF magnitude matrix. Additionally, we can further partition our LoG output to specific angles of focus, as seen in the horizontal and vertical detected filaments shown in Figs. 2(d) and 2(e). Only those pixels which contain values (i.e., not a number (NaN) values) in both LoG and OF output correspond to bending motion. The metric for bending is calculated by taking the portion of the OF vector perpendicular to the detected filament, as this measures lateral motion. To restate, from the OF vector, we are only using the component of the OF vector that is perpendicular to those filaments detected in LoG (regardless of the orientation of the filaments given from the previously described LoG output). The process is shown in the schematic and the ability to overcome crosslinking filaments

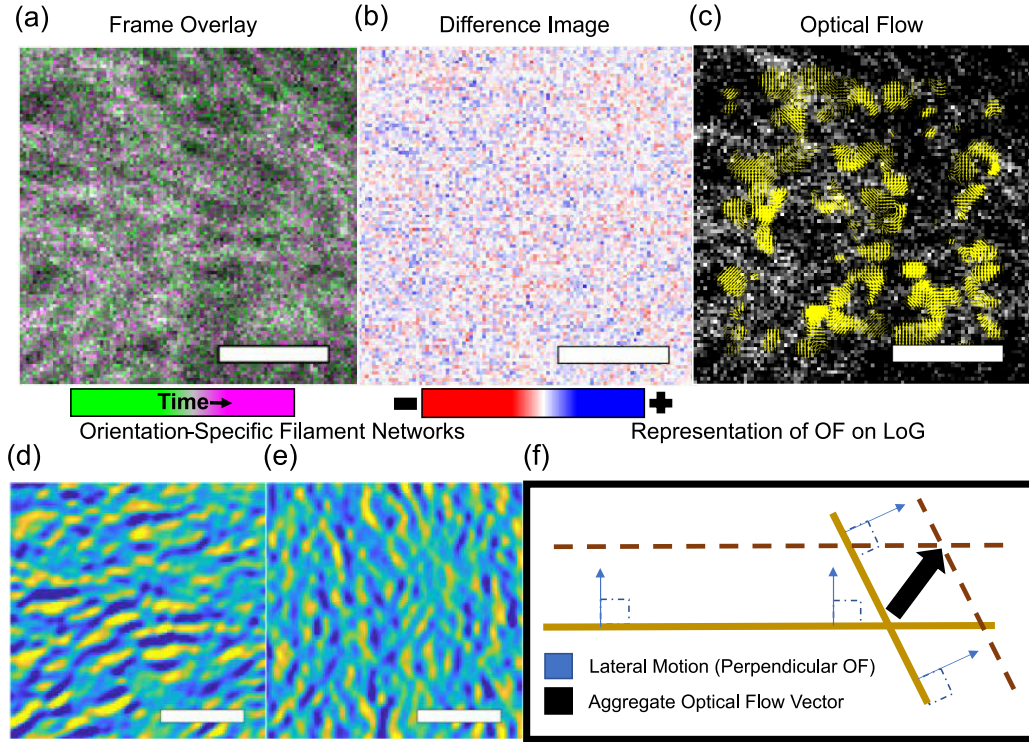


FIG. 2. Lateral motion of detected filaments is quantified by coupling OF with LoG. (a) Two frames separated by time are shown overlaid on top of each other. The minimal differences between the frames are shown by the green and magenta pixels (grayer shades—lighter from one frame, darker for the other—correspond to differences in either frame, white regions are pixels shared by both frames). (b) The frame overlay in (a) can be better represented as a difference image (a frame earlier in time subtracted from a frame later in time) where the pixels now correspond to the magnitude of intensity changes over time. (c) Using Eq. (2), we generate vectors of motion as represented by the yellow arrows [lighter regions with clusters of activity (arrows)]. Similarly to LoG, we find local neighborhoods for assessing motion. For our results, we use a kernel width, in both  $\hat{x}$  and  $\hat{y}$ , as 5. [(d), (e)] These masks showcase horizontal and vertical filaments, respectively. Notice that with our rotating LoG kernel, we are able to separately partition filaments to focus on specific orientations for analysis. (f) This schematic shows filaments in one frame (tan undashed lines) and a subsequent frame (brown dashed lines). Due to the crosslinking of filaments, the overall OF motion would normally be quantified by the larger black arrow. However, since we have access to the filament information (for which the two tan undashed lines are oriented in different directions), we can decompose that larger black vector into components perpendicular to each filament as shown by the smaller blue (lighter) arrows and analyze them separately (and we have access to the different filaments despite the crosslinking based upon the different orientation output). In this regard, we overcome the difficulty of analyzing dense MT networks and assess lateral motion. Scale bars are 3.5  $\mu\text{m}$ .

is further explained in Fig. 2(f). For this reason, we claim we are capturing the lateral motion of MTs. We achieve this by taking the sine function of the angle between the filament’s orientation and the OF vector (i.e., we take the cross product):

$$-\vec{\nabla}I \cdot \vec{v} = \frac{\partial I}{\partial t}. \tag{2}$$

**C. Manual comparison of detected motion**

To assess the reliability of our detection of the MT lateral motion, we verify outputted values with a manual estimation of movement. As shown in Fig. 3(a), the movement of the strips of data collected for CHO cells results in differences that are on the (sub)pixel level. Furthermore, the differences in between the LoG output generated from slices  $t_0$  and  $t_1$  in Fig. 3(a) are minimal, but these differences can still be seen by the eye, see Figs. 3(b) and 3(c) for comparison. To properly verify FIDI, we binarize the difference image [those values shown in neither white nor black in Fig. 3(c)] to ar-

rive at an absolute difference image. This absolute difference corresponds to overall movement of filaments. From this difference image, we use MATLAB’s regionprops function to extract an area estimate of all objects, i.e., detected objects correspond to movements of filaments across frames. Since we are interested only in the perpendicular motion of the filaments, we estimate the motion by taking the square root of all objects detected by the regionprops algorithm. We notice that our algorithm accurately captures a majority of the movement in a subpixel regime (note the lower bound of the regionprops area values is 1). We conclude that the majority of the movements correspond to the curve generated by manual estimation. See Fig. 3(d).

**D. Quantifying lateral motion to assess active forcing environments**

We use our FIDI tool to assess the active forcing environment of MTs within cells. To achieve the best possible

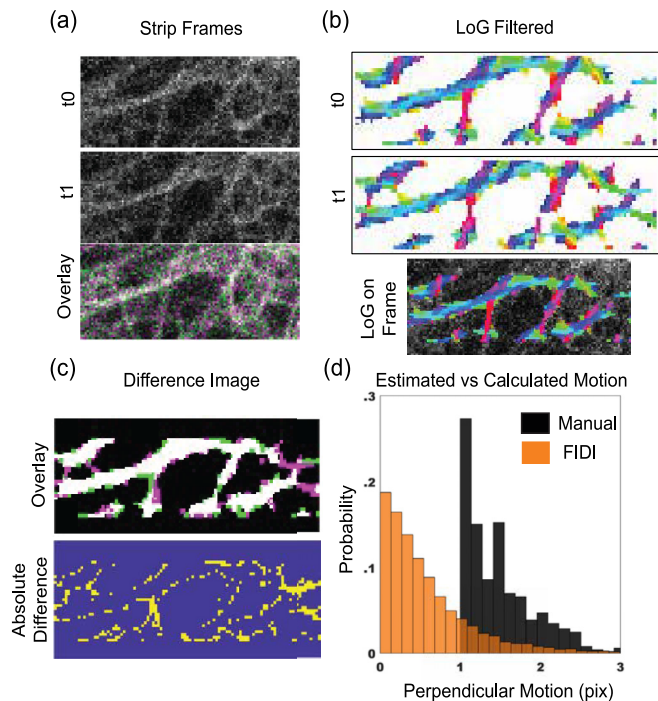


FIG. 3. Manual verification of FIDI. Comparison of the strips of CHO filaments reveals the small (sub)pixel-level movements of these clearly defined filaments. (a) Two frames at difference time points,  $t_0$  and  $t_1$ , separated vertically. The overlay of the two frames shows the differences in movement. Most of this movement is small; pixels from  $t_0$  and  $t_1$  are identified as green and magenta, respectively [shades more gray but not dark represent regions of activity from either frame; white represents regions of overlap. See (c) for more detail]. (b) For the  $t_0$  and  $t_1$  frames shown in (a), we show the LoG generated output (different colors and shades represent different angles). The slight heterogeneity of angles within the filaments is due to our pixel-level detection of filaments. Overall, however, the general angle of the filament is well-defined by eye. The LoG output overlaid below  $t_1$  showcases the agreement of our kernel parameters with the actual data. (c) To verify whether our algorithm is assessing motion with realistic output, a difference image of the detected filaments [using the LoG outputs from (b)] is generated. We further notice subpixel level differences. We quantify the area of these objects, which correspond to motion, and take the square root to mimic perpendicular motion relative to a filament. (d) We compare the values of our algorithm with a manual calculation of the square root of difference objects found. We notice that FIDI captures with subpixel-level accuracy the movements of filaments across frames.

results with our tool, we use strips of areas of CHO-K1 cells. This filament motion analysis on dense MT networks requires us to use approximately one-second frame rates and at least diffraction-limited pixel resolution. These strips are small ( $40 \text{ pix} \times 1024 \text{ pix}$  in dimension) and are not taken simultaneously. Since the cells themselves do not change shape significantly during the imaging time, and since the average location of MTs does not shift very rapidly, we combine strips corresponding to the same cell into an aggregate composite image sequence, as seen Fig. 4(a). Since each strip contains different information, we analyze each strip separately while gathering information about the entire object. This step is not a

necessary step in the FIDI algorithm. Given our strips of data, we are able to generate 24 composite CHO-K1 cells across nine independent experiments for this paper.

To further demonstrate the effects of the forcing environment on cells, we convert the angles of detected filaments to contain more biological relevance. Previous work has indicated that analyzing the orientation of filaments relative to the nearest cell boundary can determine phenotypes within a data set [20]. For each pixel, we identify its closest boundary point and then use this boundary point to determine the relative angle between the filament orientation  $\theta_{\text{fila}}$  and the vector pointing to the nearest boundary  $\theta_{\text{bound}}$ . The schematic for this conversion is shown in Fig. 4(b). Because the filament orientation is bidirectional, we choose angles smaller than or equal to  $90^\circ$ , as shown in the example output in Fig. 4(c):

$$\theta_{\text{relat}} = \min(\{\theta_{\text{bound}} - \theta_{\text{fila}}\}, \{\theta_{\text{bound}} - \theta_{\text{fila}} - \pi\}). \quad (3)$$

As the strips provide a qualitative depiction of the overall cell shape, we manually create a boundary mask for the composite cell. This allows us to quantify the overall cell boundary using this hand-drawn mask of the cell, which is used to determine the angle and distance to the nearest boundary point. The strips are analyzed separately, which limits the pixels for which we can carry out LoG filter analysis to fewer than 40 pixels wide, resulting in regions of the composite image for which we cannot determine filament orientation, as previously described. We erode the boundary mask to generate smaller regions within the composite cell so we can identify generally regions where the MTs in each strip belong globally. Each region generated for this study comprises  $1/3$  the area of the total composite cell. Each region is depicted with a different color in Fig. 4(d). The overlay of these regions on the relative angle output is shown in Fig. 4(e). Note, this regional analysis is not necessary for the overall use of FIDI, but we argue that analyzing the MTs in this fashion leads to more biologically meaningful results.

We analyze the motion of parallel and perpendicular filaments in three distinct cellular regions. We take the median value of all filaments of interest (we define perpendicular filaments as filaments whose angles relative to the cell boundary are between  $60^\circ$ – $90^\circ$ ; parallel  $0^\circ$ – $30^\circ$ ) for every frame in the composite image sequence, and then compute the mean of the transverse filament speeds for all the frames. Figure 4(f) shows a cell-by-cell comparison of transverse filament speeds for 24 cells, contrasting the motion of filaments oriented parallel or perpendicular to the nearest boundary point vector. For each cell, we compute the mean difference between these mean filament speeds for each region of the cell. As shown in Fig. 4(g), we find a small but statistically significant difference in mean lateral motion in the boundary region ( $p = 0.0305$ ). The variability in motion, measured from the variance in the mean distributions, is shown in Fig. 4(h). Across each region, we notice a more prominent downward trend in speed variability between parallel and perpendicular filaments. In Fig. 4(i), we compute the difference in speed variance for each of the three regions in the composite cells. We find that there is a small but statistically significant difference in speed variance in both the boundary ( $p = 0.0028$ ) and middle regions ( $p = 0.0306$ ). These results carry biological importance in understanding that the active forcing environment may change

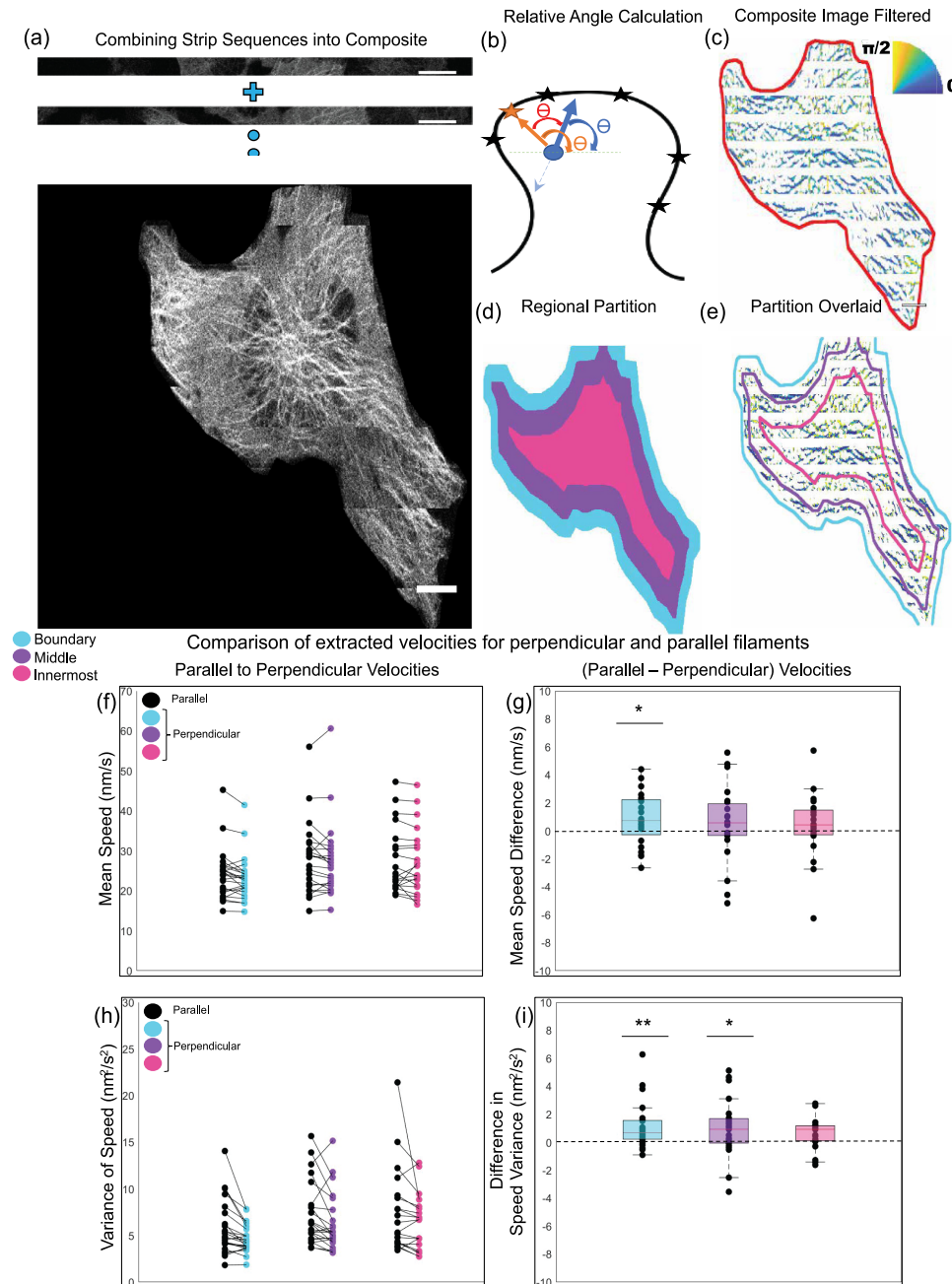


FIG. 4. Composite dynamic microtubules in CHO cells reveal differences in lateral motion based upon orientation and location. (a) Strips of CHO microtubules are taken. These strips have a higher frame rate and resolution than achieved with more standard confocal imaging. We concatenate the strips as each strip contains different information of microtubule dynamics. Despite concatenating, we separately analyze each strip to maximize the information from each cell. (b) To separate filaments into different groups, we find each filament’s orientation relative to its closest boundary point. Given a pixel’s LoG outputted angle, we find the relative angle between the angle created from the vector normal to the boundary and the unit vector created from the LoG angle. The leftmost arrow with the axis (dotted flat line) creates the boundary angle (lowermost theta). The rightmost arrow with the axis represents the filament angle. The relative angle is represented by the theta in between the two arrows. (c) The relative angle output from the composite image in (a) is shown. The color wheel displays angle colors corresponding to  $[0, \pi/2]$  (lighter shades represent perpendicular angles, darker shades represent parallel angles). (d) The composite cell image is used to generate mask from which angles relative to the boundary of the mask are generated. These regions are not meant to be exact but to provide a qualitative assessment of regional differences. (e) We show the boundaries of the regions in (d) overlaid on the output in (c). (f) We compare the mean speed of lateral motion for filaments that are considered parallel to the boundary versus filaments considered perpendicular to the boundary. We display the mean speeds side by side to demonstrate differences. From left to right: Boundary, middle, and innermost dynamics as shown in (d) above. (g) We find that only in the boundary region is there a significant difference. Filaments that are oriented parallel to the boundary seem to have a higher motion than those perpendicular. (h) We assess the variability of the mean speed across differently oriented filaments for both parallel and perpendicular filaments. We represent the difference similarly to (f). (i) We compute the difference in this variability and find a statistically significant difference in the variability in both the boundary and middle regions of the composite cells. Scale bars are 10  $\mu\text{m}$ .

depending upon location within a cell and may differently affect filaments of different orientation (e.g., in the case of torques generated within a cell acting on MTs).

#### IV. CONCLUSION

The MT network of a cell is highly dynamic mechanical structure within the cell that contains vast information regarding cellular properties. The dynamics of this information network need not be limited to the tip dynamics typically studied. As a simple readout of the dynamic state of the MT network, we have introduced a method for measuring lateral motion of MT networks that can be applied to dense networks. We argue that the lateral motions captured reflect the active forcing environments generated within a cell body. We can read out the nature of this environment via the MT network. Our method for motion analysis leverages both a rotating, anisotropic LoG filtering and optical flow by analyzing the perpendicular motion of filamentous pixels detected. We propose useful downstream analysis measures to ascertain whether angle-specific regimes work collectively or in competition with each other. We applied the technique to measure MT dynamics in CHO-K1 cells and prototyped the method on NG108 cells. We find that standard confocal microscope images have high-enough spatial resolution to reveal MT orientation, but must be acquired rapidly enough to capture MT dynamics. In CHO-K1 cells, we find statistically significant

differences between the dynamics of MTs that are tangent or normal to the closest boundary point. We also find that the dynamics depends on the distance of the MT from the cell edge.

FIDI is useful for detection of changes in MT mechanics, which is readily perturbed by a variety of chemical, mechanical, and electromagnetic probes. While our analysis cannot differentiate changes in MT stiffness from changes in active forcing due to motor proteins, FIDI provides a robust approach to characterize the cytoskeleton, complementing traditional biomechanical measurements that focus on forces and stresses such as AFM. The statistics of MT motion are also directly comparable with cellular scale simulations and can serve as an important calibration point for simulations of dynamic biomechanical structures.

The code for this paper is available at Ref. [26].

#### ACKNOWLEDGMENTS

This research was supported by funds from the Air Force Office of Scientific Research LRIR (AFOSR-LRIR No. 19RHCOR071 to I.E.). This research was initiated while N.J.M. was supported by the Repperger Research Intern Program at the Air Force Research Laboratory administered by the Oak Ridge Institute for Science and Education. This work was further supported by U.S. Air Force Office of Scientific Research Grant No. FA9550-21-1-0352 to W.L.

- 
- [1] A. Nebenführ and R. Dixit, Kinesins and Myosins: Molecular motors that coordinate cellular functions in plants, *Annu. Rev. Plant Biol.* **69**, 329 (2018).
  - [2] M. G. L. Van den Heuvel, M. P. de Graaff, and C. Dekker, Microtubule curvatures under perpendicular electric forces reveal a low persistence length, *Proc. Natl. Acad. Sci. USA* **105**, 7941 (2008).
  - [3] J. Pokorný, J. Pokorný, and J. Vrba, Generation of electromagnetic field by microtubules, *Int. J. Mol. Sci.* **22**, 8215 (2021).
  - [4] F. Pampaloni, G. Lattanzi, A. Jonáš, T. Surrey, E. Frey, and E.-L. Florin, Thermal fluctuations of grafted microtubules provide evidence of a length-dependent persistence length, *Proc. Natl. Acad. Sci. USA* **103**, 10248 (2006).
  - [5] M. G. L. van den Heuvel, S. Bolhuis, and C. Dekker, Persistence length measurements from stochastic single-microtubule trajectories, *Nano Lett.* **7**, 3138 (2007).
  - [6] A. Kis, S. Kasas, B. Babić, A. J. Kulik, W. Benoît, G. A. D. Briggs, C. Schönenberger, S. Catsicas, and L. Forró, Nanomechanics of Microtubules, *Phys. Rev. Lett.* **89**, 248101 (2002).
  - [7] A. Kis, S. Kasas, A. J. Kulik, S. Catsicas, and L. Forró, Temperature-dependent elasticity of microtubules, *Langmuir* **24**, 6176 (2008).
  - [8] M. Kikumoto, M. Kurachi, V. Tosa, and H. Tashiro, Flexural rigidity of individual microtubules measured by a buckling force with optical traps, *Biophys. J.* **90**, 1687 (2006).
  - [9] K. Wagh, M. Ishikawa, D. A. Garcia, D. A. Stavreva, A. Upadhyaya, and G. L. Hager, Mechanical regulation of transcription: Recent advances, *Trends Cell Biol.* **31**, 457 (2021).
  - [10] N. S. Rubaiya, G. Christian, N. Seiji, K. A. Md. Rashedul, S. Kazuki, Y. Takefumi, I. Mitsunori, U. Takayuki, H. Henry, and K. Akira, Deformation of microtubules regulates translocation dynamics of kinesin, *Sci. Adv.* **7**, eabf2211 (2021).
  - [11] P. Wisanpitayakorn, K. J. Mickolajczyk, W. O. Hancock, L. Vidali, and E. Tüzel, Measurement of the persistence length of cytoskeletal filaments using curvature distributions, *Biophys. J.* **121**, 1813 (2022).
  - [12] M. A. Jordan and L. Wilson, Microtubules as a target for anti-cancer drugs, *Nat. Rev. Cancer* **4**, 253 (2004).
  - [13] A. L. Parker, M. Kavallaris, and J. A. McCarroll, Microtubules and Their Role in Cellular Stress in Cancer, *Front. Oncol.* **4**, 153 (2014).
  - [14] A. L. Blajeski, V. A. Phan, T. J. Kottke, and S. H. Kaufmann, G1 and G2 cell-cycle arrest following microtubule depolymerization in human breast cancer cells, *J. Clin. Invest.* **110**, 91 (2002).
  - [15] P. Marracino, D. Havelka, J. Průša, M. Liberti, J. Tuszynski, A. T. Ayoub, F. Apollonio, and M. Cifra, Tubulin response to intense nanosecond-scale electric field in molecular dynamics simulation, *Sci. Rep.* **9**, 10477 (2019).
  - [16] A. Matov, K. Applegate, P. Kumar, C. Thoma, W. Krek, G. Danuser, and T. Wittmann, Analysis of microtubule dynamic instability using a plus-end growth marker, *Nat. Methods* **7**, 761 (2010).
  - [17] A. Zwetsloot, G. Tut, and A. Straube, Measuring microtubule dynamics, *Essays Biochem.* **62**, 725 (2018).
  - [18] R. Dhar, R. Gupta, and K. L. Baishnab, An analysis of canny and Laplacian of Gaussian image filters in regard to

- evaluating retinal image, in *Proceedings of the 2014 International Conference on Green Computing Communication and Electrical Engineering (ICGCCEE)* (IEEE, Piscataway, NJ, 2014), pp. 1–6.
- [19] J. L. Barron, D. J. Fleet, and S. S. Beauchemin, Performance of optical flow techniques, *Int. J. Comput. Vision* **12**, 43 (1994).
- [20] K. M. O’Neill, E. Saracino, B. Barile, N. J. Mennona, M. G. Mola, S. Pathak, T. Posati, R. Zamboni, G. P. Nicchia, V. Benfenati, and W. Losert, Decoding natural astrocyte rhythms: Dynamic actin waves result from environmental sensing by primary rodent astrocytes, *Adv. Biol. (Weinh)* **7**, e2200269 (2023).
- [21] R. M. Lee, L. Campanello, M. J. Hourwitz, P. Alvarez, A. Omidvar, J. T. Fourkas, and W. Losert, Quantifying topography-guided actin dynamics across scales using optical flow, *Mol. Biol. Cell* **31**, 1753 (2020).
- [22] E. Garlick, S. G. Thomas, and D. M. Owen, Super-resolution imaging approaches for quantifying F-actin in immune cells, *Front. Cell. Develop. Biol.* **9** (2021).
- [23] C. P. Brangwynne, F. C. MacKintosh, and D. A. Weitz, Force fluctuations and polymerization dynamics of intracellular microtubules, *Proc. Natl. Acad. Sci. USA* **104**, 16128 (2007).
- [24] C. P. Broedersz and F. C. MacKintosh, Modeling semiflexible polymer networks, *Rev. Mod. Phys.* **86**, 995 (2014).
- [25] W. Yang, X. Guo, S. Thein, F. Xu, S. Sugii, P. W. Baas, G. K. Radda, and W. Han, Regulation of adipogenesis by cytoskeleton remodelling is facilitated by acetyltransferase MEC-17-dependent acetylation of alpha-tubulin, *Biochem. J.* **449**, 605 (2013).
- [26] [https://github.com/losertlab/Filament\\_Displacement\\_imagetool](https://github.com/losertlab/Filament_Displacement_imagetool).